Ag@Cu2O Core-Shell Nanoparticles as Visible-Light Plasmonic Photocatalysts

8 AUTHORS, INCLUDING:

Jiangtian Li
West Virginia University

43 PUBLICATIONS **1,737** CITATIONS

SEE PROFILE

Tess R. Senty
West Virginia University

11 PUBLICATIONS **393** CITATIONS

SEE PROFILE

Peng Zheng
West Virginia University

9 PUBLICATIONS **261** CITATIONS

SEE PROFILE

Alan D Bristow
West Virginia University

108 PUBLICATIONS **1,506** CITATIONS

SEE PROFILE

Ag@Cu₂O Core-Shell Nanoparticles as Visible-Light Plasmonic Photocatalysts

Jiangtian Li,[†,‖] Scott K. Cushing,[‡,‖] Joeseph Bright,[†] Fanke Meng,[†] Tess R. Senty,[‡] Peng Zheng,[†] Alan D. Bristow,[‡] and Nianqiang Wu*[,†]

[†]Department of Mechanical and Aerospace Engineering, West Virginia University, Morgantown, West Virginia 26506-6106, United States

[‡]Department of Physics, West Virginia University, Morgantown, West Virginia 26506-6315, United States

Ⓢ *Supporting Information*

ABSTRACT: Compared to pristine Cu₂O nanoparticles (NPs), Ag@Cu₂O core-shell NPs exhibit photocatalytic activity over an extended wavelength range because of the presence of localized surface plasmon resonance (LSPR) in the Ag core. The photocatalysis action spectra and transient absorption measurements show that the plasmonic energy is transferred from the metal to the semiconductor via plasmon-induced resonant energy transfer (PIRET) and direct electron transfer (DET) simultaneously, generating electron−hole pairs in the semiconductor. The LSPR band of Ag@Cu₂O core-shell NPs shows a red-shift with an increase in the Cu₂O shell thickness, extending the light absorption of Ag@Cu₂O heterostructures to longer wavelengths. As a result, the photocatalytic activity of the Ag@Cu₂O core-shell NPs is varied by modulation of the shell thickness on the nanometer scale. This work has demonstrated that the Ag@Cu₂O core-shell heterostructure is an efficient visible-light plasmonic photocatalyst, which allows for tunable light absorption over the entire visible-light region by tailoring the shell thickness.

KEYWORDS: plasmon, photocatalyst, resonant energy transfer, electron transfer, solar energy
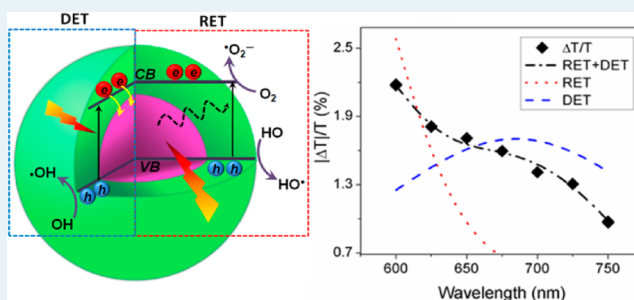
Photocatalysts convert solar energy into chemical energy to produce solar fuels or to remove pollutants. Metal oxide semiconductors are extensively used as photocatalysts.[1−5] However, many metal oxides have a wide band gap, which limits their light absorption to a small spectral region.[6−8] For example, TiO₂, which is the most common photocatalyst, only absorbs the ultraviolet light that accounts for less than 5% of all solar radiation.[7,8] Organic dye molecules[9,10] and inorganic quantum dots (QDs)[11,12] have been used as "photosensitizers" to extend the light absorption spectrum of semiconductors to enable the photocatalytic activity at longer wavelengths. Unfortunately, there is some concern about their instability.[13] An alternative to QDs and dye sensitizers is the use of plasmonic metal nanostructures combined with the metal oxide semiconductors to form plasmonic photocatalysts that utilize the plasmonic nanostructure as the sensitizer for semiconductor catalyst.[14−23] In particular, our recent report has shown that a plasmonic sensitizer can harvest and transfer solar energy to the semiconductor at the energies above and below the band edge through resonant energy transfer, which induces the charge separation, leading to the enhanced photocatalytic activity over an extended wavelength range.[14]

In the plasmonic metal, the incident radiation is converted to a nonthermalized distribution of electron−hole pairs with a lifetime of a few femtoseconds. This is an extremely short lifetime compared to conventional QD or dye sensitizers that have excited state lifetime of nanoseconds or longer. Consequently, plasmon oscillations have a broad resonance and short lifetime that allows for dramatically different energy transfer processes. Traditional QDs or dye sensitizers are based on thermalized electron transfer, in which the excited electrons relax to the band edge before transferring to the semiconductor. The process can only proceed given energetically favorable band alignment.[9,10] The energy transfer from the sensitizer to the semiconductor is a downward process, since the conduction band of the sensitizer must be aligned at a higher energy level than that of the semiconductor. In contrast, the energy transfer from a plasmonic sensitizer to a semiconductor catalyst is not restricted by electronically favorable band alignment, since the transfer may occur through a nonradiative coupling of the metal and semiconductor or charge transfer from an excited state with the energy larger than the Schottky barrier.[24,35]

The geometry plays a large role in the plasmonic energy transfer processes, which can occur even if there is a gap or an insulating medium between the catalyst and the sensitizer.[14] In contrast, semiconductor photocatalysts must be in intimate contact with the conventional QD or dye sensitizers to enable

efficient charge transfer.[12] Moreover, individual plasmonic sensitizers can be easily tuned by the local dielectric constant and/or the geometry. Thus a single sensitizer can enhance a large spectral range. Although different dyes or QDs can be used to tune the enhancement throughout the spectral region, the individual enhancement is spectrally narrow, necessitating the attachment of several different dyes or QDs to achieve full spectral coverage.

The discovery of plasmonic sensitizers has provided new opportunities to develop highly efficient photocatalysts, inspiring research in two main areas: (i) unraveling the mechanism of plasmon-enhanced photocatalysis; and (ii) optimizing the architecture for broadband absorption of solar light.

In plasmonic metal/semiconductor photocatalysts, the photoexcited plasmonic energy in the metal is transferred to the semiconductor, generating electron–hole pairs in the semiconductor.[14] Charge separation can occur either via the transfer of hot electrons known as direct electron transfer (DET)[24] or via the plasmon-induced resonant energy transfer (PIRET).[14] For DET, the nonthermalized electrons excited by a localized surface plasmon resonance (LSPR) have energy above that of the Fermi level in the metal, allowing the Schottky barrier created by charge equilibrium between the metal and the semiconductor to be overcome in the excited state.[24,35] Thus the electron transfer process does not require the energetically favorable equilibrium band alignment. In contrast, PIRET originates from a near-field electromagnetic interaction between the LSPR dipole of the metal and the interband transition dipole of the semiconductor, and therefore does not require the intimate contact between the plasmonic metal and the semiconductor.[14] Unlike DET, which has enhancement that follows the spectral shape of the LSPR, PIRET follows the spectral overlap of the LSPR and the band edge of the semiconductor. To date, DET[24] or PIRET[14] has been independently reported as being responsible for charge separation in the semiconductor. It is unclear whether DET and PIRET interact or compete with regard to the overall photocatalysis enhancement from a plasmonic sensitizer. The present work on Ag@Cu$_2$O core-shell nanoparticles (NPs) shows the previously unreported situation where DET and PIRET coexist, and both the mechanisms are responsible for the LSPR-induced charge separation in the semiconductor.

In most of the previously reported plasmonic photocatalysts, NPs were deposited on the surface of semiconductors as the isolated islands to produce a heterointerface.[25] Exposure of surface-attached metal NPs to reactants and the surrounding medium may cause corrosion and dissolution of the metal particles.[26] In addition, the metal NPs are only in point contact with the semiconductor matrix. Moreover, the observed enhancement of photocatalytic activity arises from a combination of effects due to the LSPR and self-catalysis of the metal. In the present work, metal-core@semiconductor-shell NPs are developed as plasmonic photocatalysts. The core-shell plasmonic architecture offers several advantages. First, such core-shell architecture effectively protects the metal NPs from corrosion. Second, it maximizes the metal–support interaction through the three-dimensional contact between the metal core and the semiconductor shell, thereby facilitating the plasmonic energy transfer processes. Last, the local electromagnetic field of the LSPR penetrates the shell, which can be used to tune the center wavelength of the LSPR. Specifically, the LSPR position can be tuned by changing the shell thickness on the nanometer scale. Herein photocatalytic enhancement is observed in Ag@Cu$_2$O core-shell heterostructure as a function of shell thickness since the thickness-dependent LSPR controls the synergistic contributions of PIRET and DET processes. Optimum photocatalysis can be achieved when there is broad spectral coverage. This work demonstrates, therefore, that the use of the metal-core@semiconductor-shell architecture provides flexible light harvesting that can be tailored for specific applications.

Ag NPs were synthesized by reducing AgNO$_3$ with sodium citrate (See detailed experimental section and Figure S1 in Supporting Information).[27] The Cu$_2$O shell was then coated on the Ag core to form the Ag@Cu$_2$O core@shell NPs. In this manner, the shell thickness was varied by keeping the same sized Ag cores for all samples. Briefly, 1.0 mL of as-prepared 1 mM Ag NPs solution was mixed with 5 mL of Cu^{2+} solution containing 0.1 M CuCl$_2$ and 0.0338 M sodium dodecyl sulfate (SDS) with shaking. Next, 0.15 mL of 1 M NaOH and 0.25 mL of 0.2 M NH$_4$OH·HCl were added under agitation for 10 s. The mixture was aged for 2 h and centrifuged to separate the core-shell NPs. This sample is denoted as Ag@Cu$_2$O (24 nm) according to the corresponding Cu$_2$O shell thickness. The resulting Cu$_2$O shell thickness was inversely related to the concentration of the added Ag NPs (0.25, 0.50, 1.00, 2.00, and 3.00 mL), yielding a range of 11 nm $< d <$ 40 nm (Supporting Information, Table S1). The resulting samples are denoted as Ag@Cu$_2$O (d nm). Cu$_2$O is chosen as the material for the shell because its visible-light band gap facilitates a determination of possible plasmonic energy transfer mechanisms. Cu$_2$O is initially used as a model photocatalyst to extract useful information for future development of practical photocatalyst materials.

Figure 1 shows the SEM and TEM images of Ag@Cu$_2$O (31 nm) core@shell NPs. The average diameter of well-dispersed Ag core was about 30 nm. After being coated with the Cu$_2$O shell, the total size increased to 100 nm. The Cu$_2$O shell thickness was tailored by varying the concentration of Ag NPs, as shown in Supporting Information, Table S1 and Figure S2. The LSPR positions for the various Ag@Cu$_2$O NPs in ethanol were measured with optical absorption (Figure 1d). The spectral features on the blue side of 500 nm for all samples were attributed to the interband transitions in Cu$_2$O and scattering from the Cu$_2$O shell.[32] For thicker shell NPs, the strength of the Mie scattering feature at wavelengths below 500 nm increased. The absorption feature on the red side of 500 nm was the LSPR for all the core-shell NPs. Bare Ag NPs exhibited a LSPR at 415 nm (Supporting Information, Figure S1). The local dielectric constant increased with increasing Cu$_2$O shell thickness, leading to red-shift of the peak. A curve of the LSPR position versus the shell thickness (d) was obtained by fitting the experimental data, where the fitting correlation was $R^2 =$ 0.976 (Figure 1e). Even for an 11 nm thick Cu$_2$O, the LSPR had a large red-shift due to the high refractive index of Cu$_2$O. This trend also agreed with the simulated extinction spectra calculated using the Discrete Dipole Approximation (DDA), as shown in Supporting Information, Figure S5a. The LSPR position and the plasmon field intensity are highly sensitive to both the shape and the size of the cores, as well as the dielectric constant of the surrounding medium.[28−31] Herein silver is chosen as the core material instead of gold. The plasmon frequency of pure Ag is at a higher energy than pure Au; and the plasmon dampening rate is reduced, leading to differences in the oscillator strength. The difference in the dielectric constant between Ag and Au results in different sensitivities to
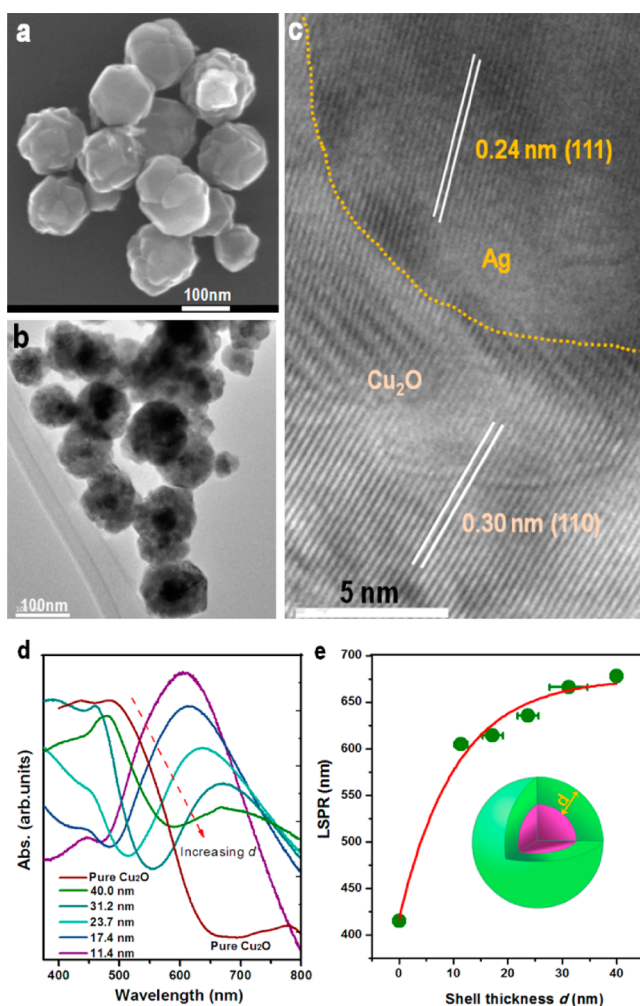
Figure 1. Microscopic images and absorption spectra of Ag@Cu₂O core-shell nanoparticles. (a) SEM, (b) TEM, and (c) HRTEM images; (d) UV−visible absorption spectra of the core-shell nanoparticles with various shell thicknesses, from left to right clearly showing the red shift of LSPR extinction; (e) the LSPR peak position as a function of the shell thickness. The Inset shows the schematic architecture of the core-shell structure.

Figure 2. Photocatalytic activity of the Ag@Cu₂O core-shell nanoparticles. (a) Degradation of methyl orange by the photocatalysts with different Cu₂O shell thicknesses; the activity was normalized with surface area; (b) and (c) the absorption spectra and the apparent photocatalytic efficiency as a function of the wavelength of monochromatic light for pure Cu₂O and Ag@Cu₂O (24 nm) nanoparticles, respectively; (d) LSPR-induced local electromagnetic field in the Cu₂O shell, the scale bar shows the relative increase in field enhancement $|E/E_{inc}|^2$. The axis refers to the physical dimensions of the core shell particle; E_{inc} is parallel to the x axis.

the effective dielectric environment resulting from the thickness of the Cu₂O shell. The higher LSPR energy of pure Ag allows for a tunable light absorption of Ag@Cu₂O over the entire visible region by changing the thickness of the Cu₂O shell. The Au@Cu₂O could not support this large tuning range. The higher LSPR energy of Ag also allows for a broader range of LSPR band overlap with the absorption band of Cu₂O.

The photocatalytic activity of the Ag@Cu₂O and the pure Cu₂O NPs were evaluated by the photodegradation rate of methyl orange (MO) in an aqueous solution under visible-light irradiation with a visible light source (Cool White Fluorescent, wavelength range from 400 to 700 nm), as shown in Figure 2. All the photocatalytic activity data were normalized with surface area; and the normalization process is given in the Supporting Information (photocatalysis section). The Ag@Cu₂O core-shell NPs showed the enhanced photocatalytic activity compared to the pure Cu₂O NPs, which can be attributed to the presence of the LSPR. The photocatalytic activity of the Ag@Cu₂O NPs was highly dependent on the shell thickness. Since increasing the Cu₂O shell thickness led to a red-shift of the LSPR, the strength of the plasmonic energy transfer depended on the shell
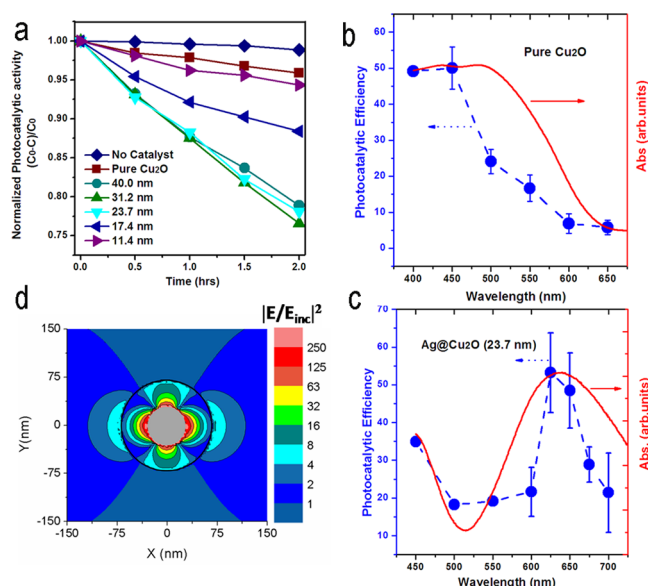
thickness. The photocatalytic activity of the Ag@Cu₂O NPs was enhanced with an increase in the shell thickness from roughly 11 to 30 nm. However, further increase in the shell thickness diminished the photocatalytic activity, as shown in Supporting Information, Figure S5.

To confirm that the LSPR was responsible for the enhancement of photocatalytic activity, the photocatalysis action spectra were obtained by plotting the apparent photocatalytic efficiency as a function of the wavelength of incident monochromatic light in the wavelength range of 450−700 nm. The apparent photocatalytic efficiency (η) per unit time was calculated according to the equation of $\eta = 1240$ eV·nm·$(C_0 - C)/C_0/(\lambda P_\lambda)$, where 1240 eV·nm units is the energy conversion factor, C_0 is the original methyl orange (MO) concentration before irradiation, C is the MO concentration after irradiation at a certain wavelength of the incident light (λ) for 3 h, P_λ is the power of monochromatic light at a certain wavelength (λ). The apparent photocatalytic efficiency does not represent a photocatalysis quantum yield, rather it is necessary to normalize the data by the differing intensity of the monochromatic light across the spectrum.

Figure 2b and 2c show the photocatalysis action spectra and the extinction spectra for the pure Cu₂O and the Ag@Cu₂O (24 nm) core@shell NPs. In both cases, the photocatalysis action spectra showed a similar trend to the extinction spectra. Pure Cu₂O exhibited negligible photocatalytic activity below the band edge, while the Ag@Cu₂O NPs displayed significant enhancement at the wavelengths corresponding to the LSPR, which was below the band gap of Cu₂O. The spectrally dependent enhancement can only happen if light excites the plasmon, and then the plasmonic energy is transferred to the semiconductor to drive the chemical reaction. Thus, this result
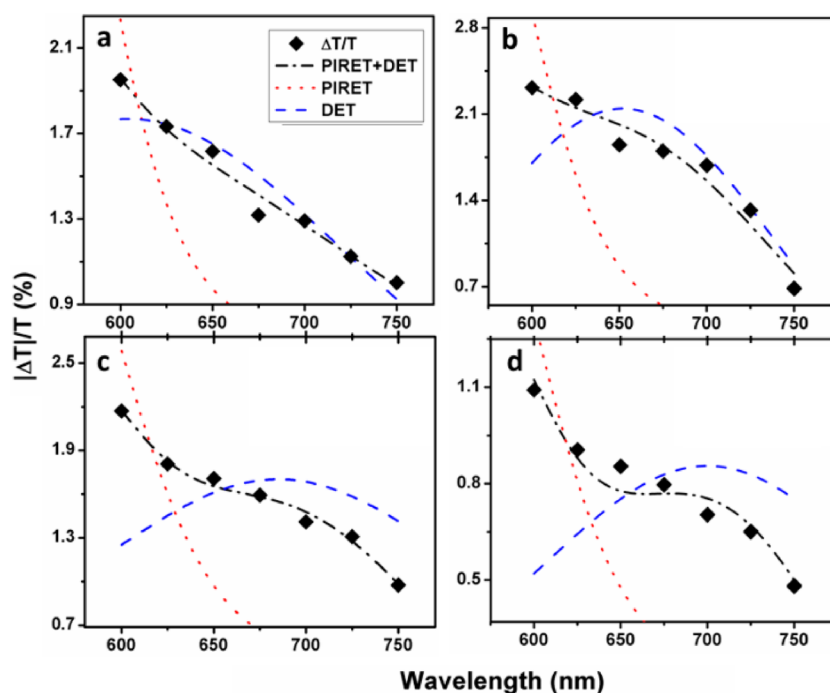
Figure 3. Transient absorption spectra and mechanism determination. $|\Delta T|/T$ versus the wavelength for (a) Ag@Cu$_2$O (11 nm), (b) Ag@Cu$_2$O (24 nm), (c) Ag@Cu$_2$O (31 nm), and (d) Ag@Cu$_2$O (40 nm). Each shell thickness is fit by a model for PIRET, DET, and PIRET+DET to show that both mechanisms are responsible for generation of charge carriers in Cu$_2$O.

confirmed that the LSPR was the most likely cause of the enhancement of photocatalytic activity. Although Fermi level equilibration can lead to trapping of charges and increased carrier lifetime, it cannot explain the observed wavelength-dependent enhancement.[26,33] This is because the charge equilibration is independent of wavelength and depends only on the electronic alignment of the Cu$_2$O and Ag. Hence, equilibration would lead to a uniform photocatalysis enhancement over the spectral range.

Photocatalysis enhancement occurred at the position of LSPR band, which indicates that the electron−hole pairs in the semiconductor can be created via DET and/or PIRET from the plasmonic metal to the semiconductor.[14] To verify that both the mechanisms were possible in the Ag@Cu$_2$O heterostructure, discrete dipole approximation simulations (DDA) of the Ag@Cu$_2$O NPs were performed by following the calculation method reported in refs 31 and 34. Figure 2d shows that the LSPR-enhanced electromagnetic (EM) field extended throughout the Cu$_2$O shell. The extent of the local EM field into the shell and the spectral overlap of the LSPR with the interband absorption band of Cu$_2$O (Supporting Information, Figure S6) satisfied the requirements for PIRET. In addition, the band alignment of Ag and Cu$_2$O allowed for the energetically favorable electron transfer, satisfying the requirements for DET. Therefore PIRET, DET, or a combination of both mechanisms may contribute to the plasmon-mediated generation of charge carriers in Cu$_2$O.

Theoretically, the carrier creation efficiency for PIRET follows the overlap integral of the Cu$_2$O absorbance and LSPR, while the carrier creation efficiency for DET follows the hot electron distribution present under excitation, and thus is represented spectrally as the LSPR absorbance.[14] Hence, separation of the two mechanisms can be achieved by measuring the wavelength-dependence of the charge carrier density in the Cu$_2$O. The carrier density was measured with

transient-absorption spectroscopy, which was performed with 100-fs pump and probe pulses. The pump was tuned across the spectral region of interest from 600 to 750 nm and the probe was centered at 800 nm, such that it was predominantly sensitive to free-carrier absorption in the Cu$_2$O. The amplitude of the differential transmission $|\Delta T|/T$ was extracted for each pump wavelength at a probe delay of approximately 10 ps. This delay time was determined from the transients (Supporting Information, Figure S7) to correspond with the $|\Delta T|/T$ response shortly after the decay of the transient contribution from the Ag core but before recombination in Cu$_2$O significantly affected the carrier population. Figure 3 shows the wavelength-dependent carriers concentration for the Ag@Cu$_2$O NPs with four different shell thicknesses: 11, 24, 31, and 40 nm. In each case, the carrier density was largest at shorter wavelength, close to the absorption edge of Cu$_2$O, and decreased at longer wavelengths below the interband absorption. For the chosen 800-nm probe, neither the pure Cu$_2$O or the Ag NPs exhibited transient signals. Therefore, the observed differential transmission from the Ag@Cu$_2$O NPs was due to plasmon-induced carrier accumulation in Cu$_2$O.

To determine whether DET or PIRET dominated the plasmonic-energy transfer to the Cu$_2$O, a model was produced for the spectra signature of each mechanism. The UV−visible spectrum for each sample was deconvolved into contributions from the LSPR and the Cu$_2$O interband absorption (Supporting Information, Figure S6). PIRET followed the overlap integral between these two components, while DET followed the LSPR. The two contributions were used in conjunction to fit the wavelength-dependent differential transmission (see Figure 3). The fitting procedure confirmed that both PIRET and DET were necessary to describe the data for all shell thicknesses measured. Nonetheless, as the Cu$_2$O shell thickness increased, the relative contribution of DET and PIRET was different. For the thin shell sample, DET and

PIRET contributions overlapped strongly since the peak of the LSPR was located close to the Cu_2O absorption edge (Figure 3a). For the three thicker samples, the red shift of the LSPR was significantly larger, which separated the PIRET and DET contributions (Figure 3b-d). Overall, these three samples exhibited stronger photocatalytic activity and thus presented a couple of striking factors. First, these data reveal the wide tuning range of the LSPR, while maintaining enhancement of the photocatalytic activity. Second, strong photocatalytic activity were observed even for weak overlap between the LSPR and the Cu_2O absorption edge. Finally, DET and PIRET complemented one another in the enhancement of the photocatalytic activity. In contrast, the thinner sample did not show significant enhancement of photocatalytic activity when the DET and PIRET processes strongly overlapped, which suggested that the mechanisms may compete in this case. There existed an optimal shell thickness for maximizing the overall visible-light photocatalytic activity (Figure 2a and Supporting Information, Figure S5). Several factors competed to define the optimal thickness, as analyzed in the Supporting Information.

In summary, the metal core@semiconductor shell architecture exhibited the plasmonic enhancement of visible-light photocatalytic activity. The entire visible-light spectrum can be enhanced by tuning the shell thickness, or a specific spectral region can be targeted. Transient absorption measurements showed that both PIRET and DET mechanisms contributed to the plasmonic energy transfer from the metal to the semiconductor, leading to charge separation in the Cu_2O. The Ag@Cu_2O core-shell structure was an efficient visible-light plasmonic photocatalyst with the flexibility for tailoring the plasmonic properties and also an ideal platform for mechanistic studies of the plasmonic energy transfer from a metal to a semiconductor. The plasmonic energy transfer mechanisms outlined in this study can be extended to any metal-semiconductor interaction, not just Cu_2O, outlining the design strategies for plasmonic enhancement of photocatalysis.

ASSOCIATED CONTENT

Ⓢ Supporting Information

Experimental details, SEM and TEM images for Ag@Cu_2O nanoparticles, photocatalytic kinetic data, DDSCAT simulation, and transient absorption spectroscopy. This material is available free of charge via the Internet at http://pubs.acs.org.

AUTHOR INFORMATION

Corresponding Author

*Fax: (+1) 304-293-6689. E-mail: nick.wu@mail.wvu.edu.

Author Contributions

‖Li and Cushing contributed equally to this work.

Notes

The authors declare no competing financial interest.

ACKNOWLEDGMENTS

REFERENCES

(1) Maeda, K.; Domen, K. *J. Phys. Chem. Lett.* **2010**, *1*, 2655.
(2) Kudo, A.; Miseki, Y. *Chem. Soc. Rev.* **2009**, *38*, 253.
(3) Wu, N. Q.; Wang, J.; Tafen, D.; Wang, H.; Zheng, J. G.; Lewis, J. P.; Liu, X.; Leonard, S. S.; Manivannan, A. *J. Am. Chem. Soc.* **2010**, *132*, 6679.
(4) Li, J.; Meng, F.; Suri, S.; Ding, W.; Huang, F.; Wu, N. Q. *Chem. Commun.* **2012**, *48*, 8213.
(5) Meng, F.; Hong, Z.; Arndt, J.; Li, M.; Zhi, M.; Yang, F.; Wu, N. Q. *Nano Res.* **2012**, *5*, 213.
(6) Meng, F.; Li, J.; Hong, Z.; Sakla, A.; Wu, N. Q. *Catal. Today* **2013**, *199*, 48−52.
(7) Wang, J.; Tafen, D.; Lewis, J. P.; Hong, Z.; Manivannan, A.; Zhi, M.; Li, M.; Wu, N. Q. *J. Am. Chem. Soc.* **2009**, *131*, 12290.
(8) Tafen, D.; Wang, J.; Wu, N. Q.; Lewis, J. P. *Appl. Phys. Lett.* **2009**, *94*, 093101.
(9) Youngblood, W. J.; Lee, S.H. A.; Maeda, K.; Mallouk, T. E. *Acc. Chem. Res.* **2009**, *42*, 1966.
(10) Ni, M.; Leung, M. K.H.; Leung, D. Y.C.; Sumathy, K. *Renewable Sustainable Energy Rev.* **2007**, *11*, 401.
(11) Li, G.; Zhang, D.; Yu, J. C. *Environ. Sci. Technol.* **2009**, *43*, 7079.
(12) Wang, D.; Zhao, H.; Wu, N. Q.; El Khakani, A.; Ma, D. *J. Phys. Chem. Lett.* **2010**, *1*, 1030.
(13) Wang, B.; Kerr, L. L. *J. Solid State Electrochem.* **2012**, *16*, 1091.
(14) Cushing, S. K.; Li, J.; Meng, F.; Senty, T. R.; Suri, S.; Zhi, M.; Li, M.; Bristow, A. D.; Wu, N. Q. *J. Am. Chem. Soc.* **2012**, *134*, 15033.
(15) Ide, Y.; Matsuoka, M.; Ogawa, M. *J. Am. Chem. Soc.* **2010**, *132*, 16762.
(16) Naya, S.; Inoue, A.; Tada, H. *Energy Environ. Sci.* **2012**, *5*, 5133.
(17) Awazu, K.; Fujimaki, M.; Rockstuhl, C.; Tominaga, J.; Murakami, H.; Ohki, Y.; Yoshida, N.; Watanabe, T. *J. Am. Chem. Soc.* **2008**, *130*, 1676.
(18) Hu, C.; Peng, T.; Hu, X.; Nie, Y.; Zhou, X.; Qu, J.; He, H. *J. Am. Chem. Soc.* **2010**, *132*, 857.
(19) Christopher, P.; Ingram, D. B.; Linic, S. *J. Phys. Chem. C* **2010**, *114*, 9173.
(20) Ingram, D. B.; Linic, S. *J. Am. Chem. Soc.* **2011**, *133*, 5202.
(21) Thomann, I.; Pinaud, B. A.; Chen, Z.; Clemens, B. M.; Jaramillo, T. F.; Brongersma, M. L. *Nano Lett.* **2011**, *11*, 3440.
(22) Liu, Z.; Hou, W.; Pavaskar, P.; Aykol, M.; Cronin, S. B. *Nano Lett.* **2011**, *11*, 1111.
(23) Thimsen, E.; Formal, F.; Grätzel, M.; Warren, S. C. *Nano Lett.* **2011**, *11*, 35.
(24) Tian, Y.; Tatsuma, T. *J. Am. Chem. Soc.* **2005**, *127*, 7632.
(25) Murdoch, M.; Waterhouse, G. I. N.; Nadeen, M. A.; Metson, J. B.; Keane, M. A.; Howe, R. F.; Liorca, J.; Idriss, H. *Nat. Chem.* **2011**, *3*, 489.
(26) Hirakawa, T.; Kamat, P. *J. Am. Chem. Soc.* **2005**, *127*, 3928.
(27) Lee, P. C.; Meisel, D. *J. Phys. Chem.* **1982**, *86*, 3391.
(28) Liu, D.; Ding, S.; Lin, H.; Liu, B.; Ye, Z.; Fan, F.; Ren, B.; Tian., Z. *J. Phys. Chem. C* **2012**, *116*, 4477.
(29) Zhang, L.; Wang, H. *ACS Nano* **2011**, *5*, 3257.
(30) Zhang, L.; Blom, D. A.; Wang, H. *Chem. Mater.* **2011**, *23*, 4587.
(31) Li, M.; Cushing, S. K.; Zhang, J.; Lankford, J.; Aguilar, Z. P.; Ma, D.; Wu, N. Q. *Nanotechnology* **2012**, *23*, 115501.
(32) Mahmoud, M.; Qian, W.; El-Sayed, M. *Nano Lett.* **2011**, *11*, 3285.
(33) Wolf, E. F.; Kamat, P. V. *J. Am. Chem. Soc.* **2004**, *126*, 4943.
(34) Cushing, S. K.; Hornak, L. A.; Lankford, J.; Liu, Y.; Wu, N. Q. *Appl. Phys. A: Mater. Sci. Process.* **2011**, *103*, 955.
(35) Furube, A.; Du, L.; Hara, K.; Katoh, R.; Tachiya, M. *J. Am. Chem. Soc.* **2007**, *129*, 14852.

Ag@Cu₂O Core-Shell Nanoparticles as Visible-Light Plasmonic Photocatalysts

Jiangtian Li,† # Scott K. Cushing, ‡,# Joeseph Bright,† Fanke Meng,† Tess R. Senty,‡ Peng Zheng,† Alan D. Bristow, ‡ and Nianqiang Wu†,*

†Department of Mechanical and Aerospace Engineering, West Virginia University, Morgantown, WV 26506-6106, USA

‡Department of Physics, West Virginia University, Morgantown, WV 26506-6315, USA

# Li and Cushing contributed equally to this work

*Corresponding author: Tel: +1-304-293-3326; Fax: +1-304-293-6689; E-mail: nick.wu@mail.wvu.edu.

Experimental Details

Synthesis of Ag nanoparticles (NPs)

The Ag NPs with an average size of 30 nm were prepared by sodium citrate reducing AgNO₃ aqueous solution.[1] Typically, 150 mL of 1 mM AgNO₃ was heated to the boiling point, and then 10 mL of 1 wt% sodium citrate was quickly added. The mixture was then kept at boiling for half an hour, yielding the gray yellow Ag NPs. The absorption spectrum of Ag NPs colloid was shown in Figure S1, and LSPR peak was located at around 415 nm.

Synthesis of Ag@Cu₂O core-shell NPs

The Ag@Cu₂O core-shell plasmonic photocatalysts were synthesized by following the reported procedure for the synthesis of Au@Cu₂O.[2] Typically, 1.0 mL of as-prepared 1 mM Ag NP solution was added into 5 mL of Cu²⁺ solution containing 0.1 M CuCl₂ and 0.0338 M sodium dodecyl sulfate (SDS) with shaking. Next 0.15 mL of 1 M NaOH and 0.25 mL of 0.2 M NH₂OH·HCl were added with shaking for 10 seconds. The mixture was aged for 2 h and centrifuged to separate the core-shell NPs. This as-prepared sample was named as Ag@Cu₂O (24 nm) according to Cu₂O shell thickness. If not otherwise specified, all Ag@Cu₂O samples were named in this way. The Cu₂O shell thickness can be tuned by varying the addition amount of Ag NPs, the corresponding thickness for all samples were listed in Table **S1**.

Characterization

The morphology of Ag@Cu₂O core-shell structures was observed with a field-emission scanning electron microscope (FE-SEM) (JEOL 7600F). The light-absorption properties were characterized by the diffuse-reflection mode with Shimadzu 2550 UV-Visible spectrometer equipped with an integrating sphere (UV 2401/2, Shimadzu).

Experimental Details

Synthesis of Ag nanoparticles (NPs)

The Ag NPs with an average size of 30 nm were prepared by sodium citrate reducing $AgNO_3$ aqueous solution.[1] Typically, 150 mL of 1 mM $AgNO_3$ was heated to the boiling point, and then 10 mL of 1 wt% sodium citrate was quickly added. The mixture was then kept at boiling for half an hour, yielding the gray yellow Ag NPs. The absorption spectrum of Ag NPs colloid was shown in Figure S1, and LSPR peak was located at around 415 nm.

Synthesis of Ag@Cu$_2$O core-shell NPs

The Ag@Cu_2O core-shell plasmonic photocatalysts were synthesized by following the reported procedure for the synthesis of Au@Cu_2O.[2] Typically, 1.0 mL of as-prepared 1 mM Ag NP solution was added into 5 mL of Cu^{2+} solution containing 0.1 M $CuCl_2$ and 0.0338 M sodium dodecyl sulfate (SDS) with shaking. Next 0.15 mL of 1 M NaOH and 0.25 mL of 0.2 M $NH_2OH·HCl$ were added with shaking for 10 seconds. The mixture was aged for 2 h and centrifuged to separate the core-shell NPs. This as-prepared sample was named as Ag@Cu_2O (24 nm) according to Cu_2O shell thickness. If not otherwise specified, all Ag@Cu_2O samples were named in this way. The Cu_2O shell thickness can be tuned by varying the addition amount of Ag NPs, the corresponding thickness for all samples were listed in Table **S1**.

Characterization

The morphology of Ag@Cu_2O core-shell structures was observed with a field-emission scanning electron microscope (FE-SEM) (JEOL 7600F). The light-absorption properties were characterized by the diffuse-reflection mode with Shimadzu 2550 UV-Visible spectrometer equipped with an integrating sphere (UV 2401/2, Shimadzu).

Measurement of photocatalytic activity under UV and visible-light irradiation

The photocatalytic activity of the samples was evaluated by the degradation of methyl orange in an aqueous solution under the irradiation of visible-light at ambient temperature and pressure. A commercial photoreactor (LUZ-4 V, Luzchem) equipped with fourteen 8 W visible (Cool white Florescent, wavelength range from 400-700 nm) was used as visible-light sources to trigger the photocatalytic reactions. Typically, four standard samples were dispersed in 100 mL of 15 mg/L methyl orange (MO), and were ultrasonicated for 15 min and stirred for 3 hours in dark to reach an adsorption/desorption equilibrium. 5 mL of samples solution was drawn from the system at a certain time interval during the experiment, and then centrifuged to analyze the residual amount of MO using a Shimadzu UV-vis spectrophotometer. The percentage of degradation was calculated by $(C_0 - C)/C_0$, where C is the absorption of MO solution at each irradiation time interval, and C_0 is the absorption of the initial concentration when the adsorption-desorption equilibrium was achieved.

Wavelength dependent photocatalytic activity under monochromatic light

To evaluate the correlation between the photocatalytic activity and the wavelength, the photocatalytic activities of samples were measured under the monochromatic light using a 300 W Xe lamp as the light source coupled with a monochromator (Oriel Cornerstone 130 1/8m). Typically, four standard samples were dispersed in 150 mL of 15 mg/L methyl orange, and were ultrasonicated for 15 min and stirred for 3 hours in dark to reach an adsorption/desorption equilibrium. The samples were contained in a quartz cell and exposed in monochromatic light. During the process, the solution was kept stirring. After exposure for 3 hours, the solution was centrifuged to analyze the residual amount of MO.

Normalization of the photocatalytic activity based on the surface area

The photocatalytic activity of Ag@Cu$_2$O core-shell NPs with different Cu$_2$O shell thicknesses was normalized based on the surface area. The same amount but the different

thickness of Cu_2O shell leads to the different surface areas for different $Ag@Cu_2O$ core-shell NPs. The normalization was carried out using the equation $4\pi R^2 n$, where R and n present the radius, and numbers of the corresponding $Ag@Cu_2O$ NPs, respectively. As shown in TEM image, each Ag NP was wrapped with Cu_2O and no pure Cu_2O was detected, so n is equal to the amount of Ag NPs. The surface area of $Ag@Cu_2O$ (11 nm) was supposed to be 1 and the ratios of other samples compared to $Ag@Cu_2O$ (11 nm) were calculated and listed in Table S1. Pure Cu_2O display a cubic morphology with an edge length of 108 nm, its surface area compared to $Ag@Cu_2O$ (11 nm) was also listed in Table S1.

Discrete dipole approximation simulations

Simulation of the local electromagnetic field was performed using the open source DDSCAT code.[3] DDSCAT utilizes the discrete dipole approximation to simulate the absorption, scattering, and extinction of geometry by assuming it is composed of a discrete set of dipoles. The electromagnetic field and scattering are then calculated based on the interaction of each dipole with the incident field and surrounding dipoles. The core shell structures were modeled using the core/shell geometry with an interdipole spacing of 0.3 nm. The refractive index for Cu_2O and Ag was taken from Palik[4] and the online Sopra N and K database. The input source was at the plasmon peak for each shell thickness and linearly polarized along the X direction.

Transient absorption spectroscopy

Non-degenerate pump-probe experiments were performed with 100-fs pulses from a 1 KHz Ti:sapphire laser amplifier (Libra) and an optical parametric amplifier (OPerA Solo). Pump pulses from the OPerA Solo where doubled in a β-barium borate crystal to provide a tunable wavelength source from 600 nm to 750 nm. Probe pulses were taken directly from the Libra. Time-delay between the pulses was controlled by a motion control system with a 3-ns time range. Focused beam spot sizes were 400 μm for the pump and 240 μm for the probe. Samples were dispersed in a KBr matrix. Transmission probe radiation was monochromated, collected on a photo-detector, and recorded with a lock-in amplifier.

Table s1. Data summary for Ag@Cu$_2$O core-shell nanoparticles with different Cu$_2$O shell thicknesses.

Sample	Volume of Ag NPs (mL)	Shell thickness, d (nm)	Normalized surface area
Ag@Cu$_2$O (40 nm)	0.25	40	1
Ag@Cu$_2$O (31 nm)	0.50	31.2	1.41
Ag@Cu$_2$O (24 nm)	1.00	23.7	1.98
Ag@Cu$_2$O (17 nm)	2.00	17.4	2.77
Ag@Cu$_2$O (11 nm)	3.00	11.4	2.76
Pure Cu$_2$O	0	0	0.99
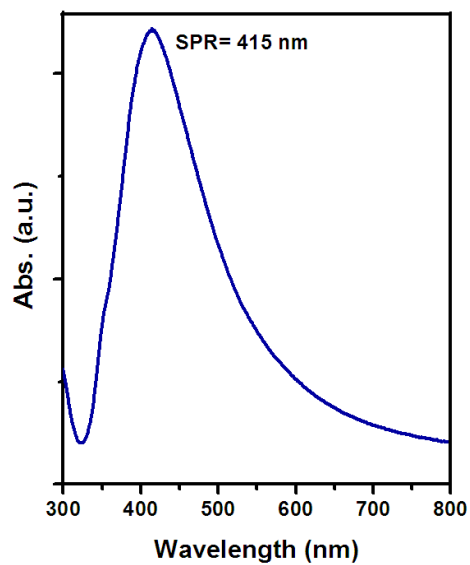
Figure S1. UV-Visible absorption spectrum for the Ag nanoparticles. The LSPR peak of the Ag nanoparticles is located at 415 nm.
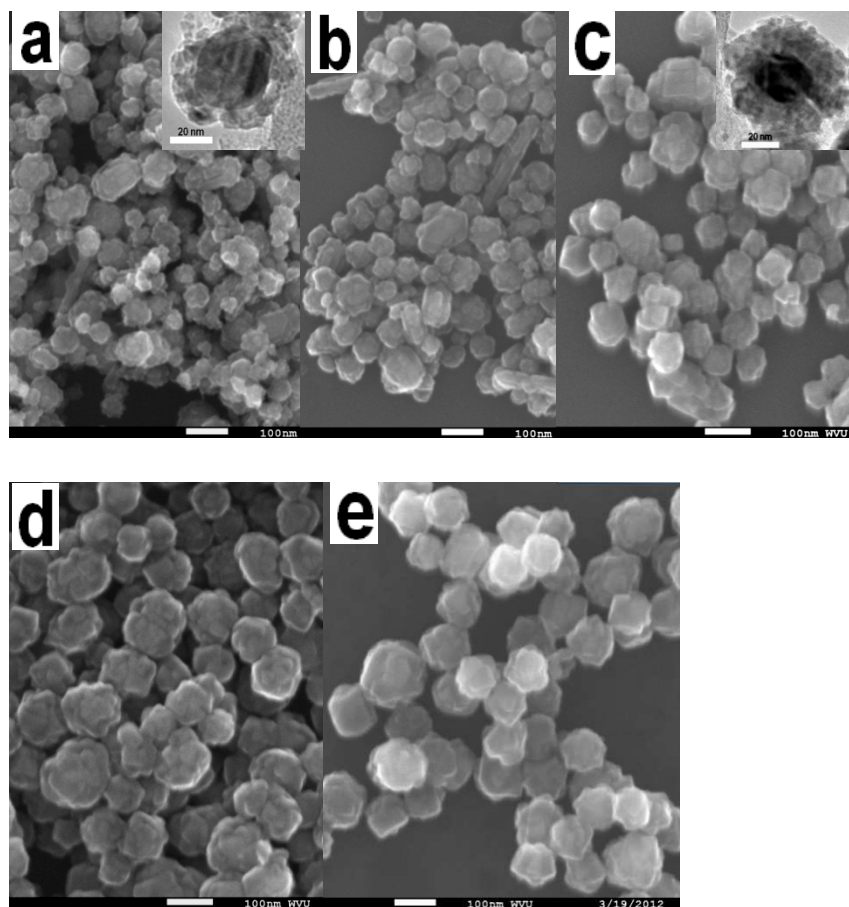
Figure S2. The morphology of Ag@Cu$_2$O with different Cu$_2$O shell thicknesses. (a) Ag@Cu$_2$O (d=11 nm), (b) Ag@Cu$_2$O (d=17 nm), (c) Ag@Cu$_2$O (d=24 nm), (d) Ag@Cu$_2$O (d=31 nm), and (e) Ag@Cu$_2$O (d=40 nm), respectively. The insets in (a) and (c) present the corresponding TEM images.
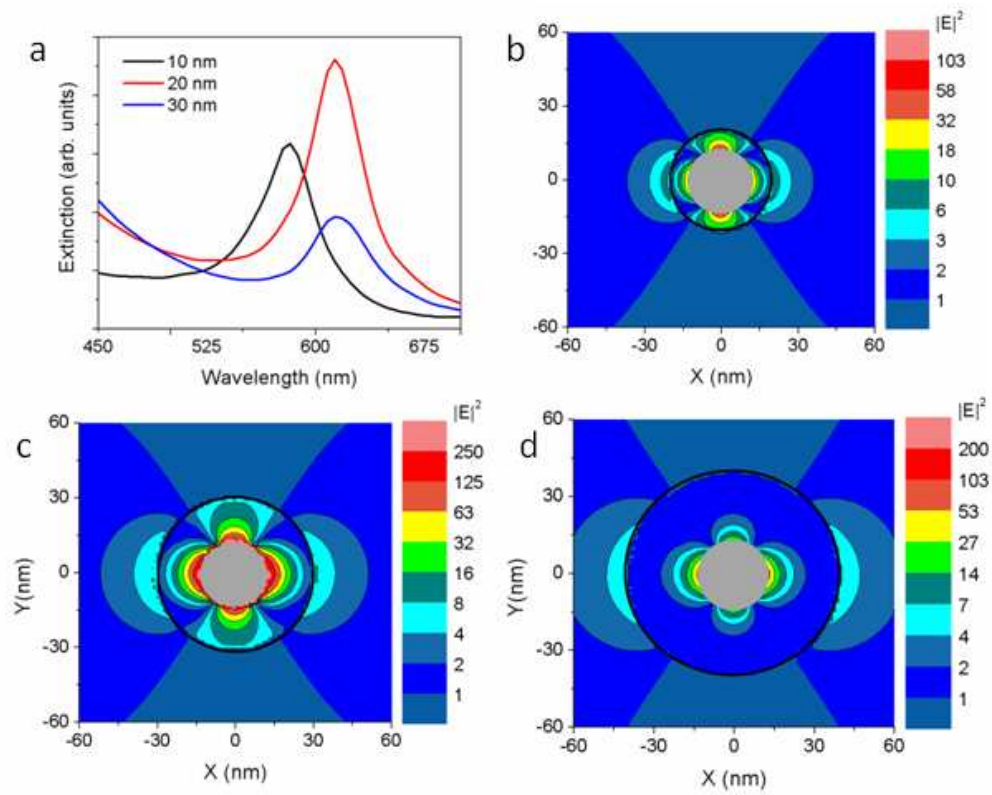
Figure S3. Discrete dipole approximation simulations for (a) the extinction spectrum and the electromagnetic field enhancement $|E\backslash E_0|^2$ for (b) 10 nm, (c) 20 nm, and (d) 30 nm Cu_2O shells.
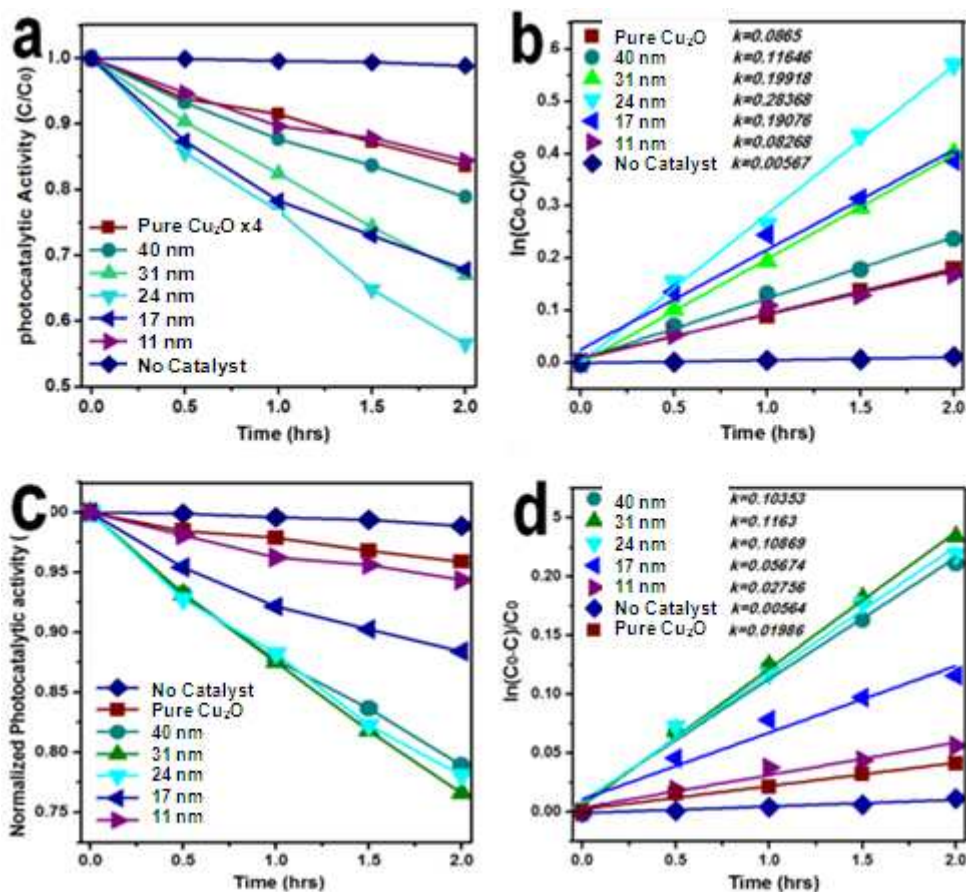
Figure S4. Photocatalytic degradation activity of Ag@Cu$_2$O over methyl orange with different Cu$_2$O shell thickness. *a* and *c* show the photodegradation of MO calculated with (C$_o$-C)/C$_0$, *b* and *d* present the corresponding kinetic study with a linear fitting, ln(C$_o$-C)/C$_0$=a+kt, where k is the apparent first-order rate constant. The degradation of MO can be ascribed to a pseudo-first-order reaction with a simplified Langmuir-Hinshelwood model. The concentration of pure Cu$_2$O is 4 times higher than that for Ag@Cu$_2$O NPs samples in *a* and *b*. All the data were then normalized with the surface area for samples with different shell thickness, and displayed in *c* and *d*. The normalization process was enclosed in experimental section.
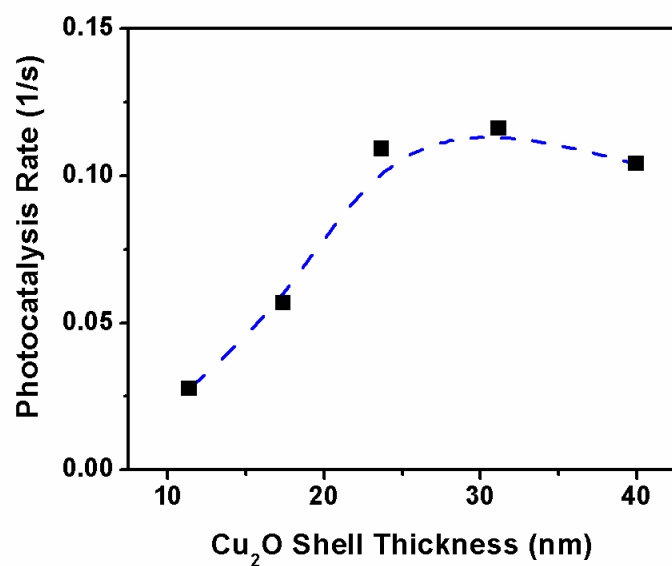
Figure S5. Photocatalytic degradation rate of Ag@Cu$_2$O over methyl orange versus the Cu$_2$O shell thickness. The Kinetic rate was taken from Figure S3.
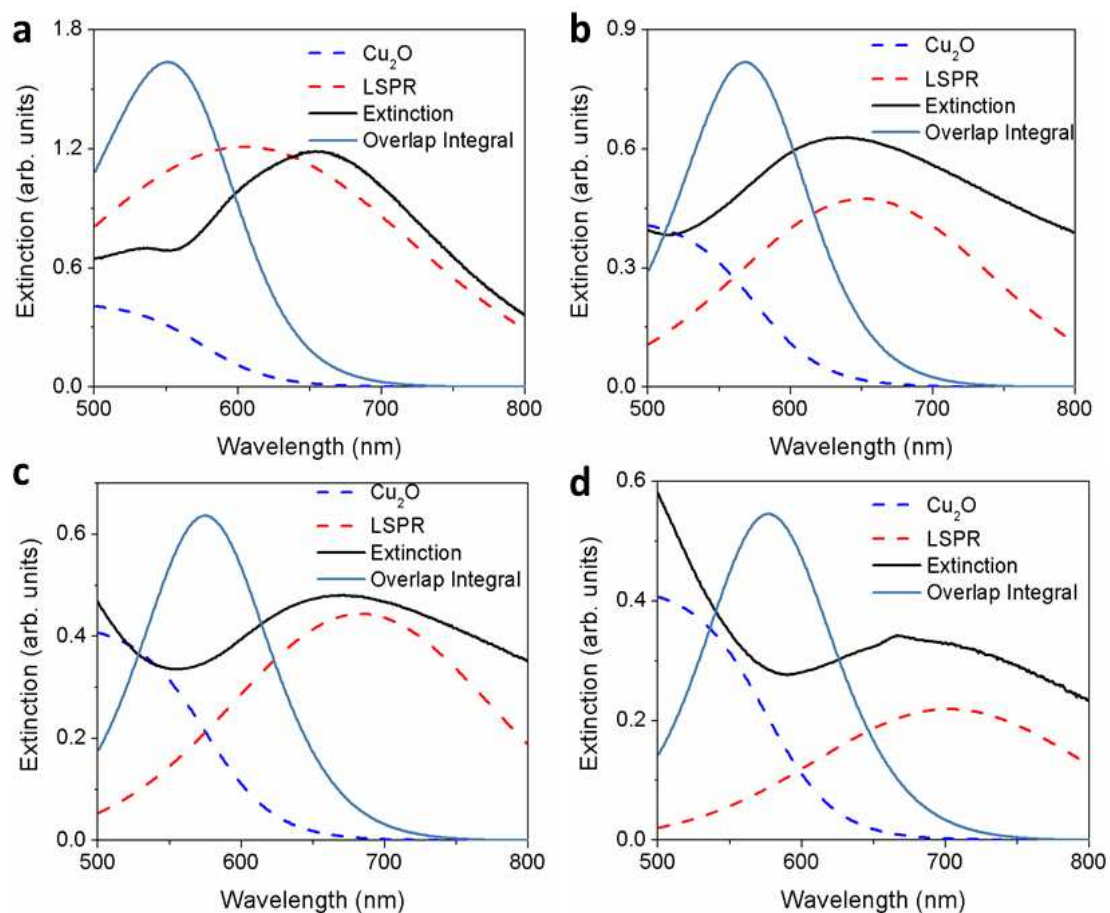
Figure S6. Overlap function for Ag@Cu₂O core-shell nanoparticles. The UV-Vis extinction for the core shell particle, the modeled Cu₂O and LSPR absorption, and calculated overlap integral for (a) Ag@Cu₂O (11 nm), (b) Ag@Cu₂O (24 nm), (c) Ag@Cu₂O (31 nm), and (d) Ag@Cu₂O (40 nm).
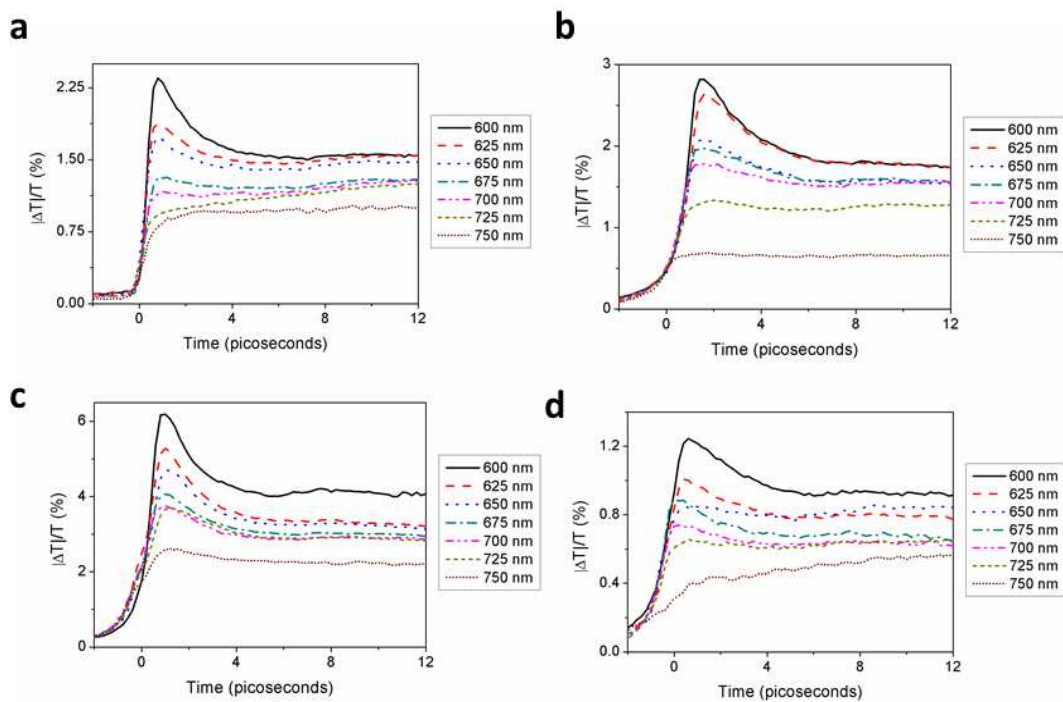
Figure S7. Transient absorption spectra obtained from the Ag@Cu$_2$O core-shell nanoparticles for (a) Ag@Cu$_2$O (11 nm), (b) Ag@Cu$_2$O (24 nm), (c) Ag@Cu$_2$O (31 nm), and (d) Ag@Cu$_2$O (40 nm) at varying wavelengths. The relative number of carriers is proportional to the differential transmission at 10 picoseconds where the dynamics due to the noble metal have decayed.

Analysis of optimal shell thickness for overall visible-light photocatalytic activity

There existed an optimal shell thickness for maximizing the overall visible-light photocatalytic activity (Figure 2a and Figure S5). Several factors compete to define the optimal thickness. First, since increasing the Cu_2O shell thickness leads to a red-shift of the LSPR peak, the strength of the plasmonic energy transfer depends on the shell thickness. Second, although the local EM field was extended into the Cu_2O shell for all shell thicknesses tested (Figure S3), the intensity of the plasmonic enhancement ($|E/E_0|^2$) was different. The plasmonic enhancement was largest for the 20 nm thick shell and decreased for thinner or thicker shells. The local EM field did not completely decay for the 10 nm thick shell, suggesting incomplete coupling. Finally, change in the shell thickness affects the recombination of the LSPR-induced electron and holes. Very thin Cu_2O shell thickness will influence the lifetimes of charge carriers due to an increase in the surface states as compared to bulk states, possibly reducing the photocatalytic efficiency. As the shell thickness increases, the carrier recombination dynamics becomes closer to that of bulk Cu_2O. All of these factors contribute to the dependency of photocatalytic enhancement on thickness. The strength of the plasmonic energy transfer and the resulting photocatalysis enhancement are proportional to the strength of the LSPR and the coupling of the near field EM interaction as well as the carrier lifetime, suggesting why the photocatalysis is optimized for shell thicknesses of around 20-30 nm.

References

1. Lee, P. C.; Meisel, D. *J. Phys. Chem.*, 1982, 86, 3391.

2. Kuo, C.H.; Hua, T.; Huang, M. H. *J. Am. Chem. Soc.*, 2009, 131, 17871–17878.

3. Draine, B.T.; Flatau, P. J. *J. Opt. Soc. Am.* 1994, *A11*, 1491-1499.

4. Palik, E. D. Handbook of Optical Constants of Solids; Academic Press: Boston, 1985.